

JMBAvailable online at www.sciencedirect.com ScienceDirect

Polymorphic Assemblies and Crystalline Arrays of Lens Tetraspanin MP20

Tamir Gonen^{1,2*}, Richard K. Hite², Yifan Cheng², Benjamin M. Petre²
Joerg Kistler¹ and Thomas Walz^{2*}

¹*School of Biological Sciences
University of Auckland
Auckland, New Zealand*

²*Department of Cell Biology
Harvard Medical School
Boston, MA 02115, USA*

Received 1 May 2007;
received in revised form
29 August 2007;
accepted 3 September 2007
Available online
8 September 2007

Members of the tetraspanin superfamily function as transmembrane scaffold proteins that mediate the assembly of membrane proteins into specific signaling complexes. Tetraspanins also interact with each other and concentrate membrane proteins into tetraspanin-enriched microdomains (TEMs). Here we report that lens-specific tetraspanin MP20 can form multiple types of higher-order assemblies and we present crystalline arrays of MP20. When isolated in the absence of divalent cations, MP20 is solubilized predominantly in tetrameric form, whereas the presence of divalent cations during solubilization promotes the association of MP20 tetramers into higher-order species. This effect only occurs when divalent cations are present during solubilization but not when divalent cations are added to solubilized tetrameric MP20, suggesting that other factors may also be involved. When purified MP20 tetramers are reconstituted with native lens lipids in the presence of magnesium, MP20 forms two-dimensional (2D) crystals. A projection map at 18 Å resolution calculated from negatively stained 2D crystals showed that the building block of the crystal is an octamer consisting of two tetramers related to each other by 2-fold symmetry. In addition to 2D crystals, reconstitution of MP20 with native lipids also produced a variety of large protein–lipid complexes, and we present three-dimensional (3D) reconstructions of the four most abundant of these complexes in negative stain. The various complexes formed by MP20 most likely reflect the many ways in which tetraspanins can interact with each other to allow formation of TEMs.

© 2007 Published by Elsevier Ltd.

Edited by W. Baumeister

Keywords: MP20; tetraspanin; tetraspanin-enriched microdomains; two-dimensional crystal; single particle electron microscopy

Introduction

Tetraspanins form a superfamily of abundantly expressed transmembrane proteins that are conserved from schistosomes and some fungi to mammals.¹ The tetraspanin superfamily contains at least 35 members in flies, 20 in worms and 32 in mammals. Tetraspanins are characterized by four membrane-spanning domains, a large extracellular loop (LEL) containing a conserved CCG motif, a second smaller extracellular loop and short cytoplasmic amino and carboxy termini.² Members of the tetraspanin family have been implicated in a wide range of cellular functions including adhesion, migration, synapse formation, intracellular protein transport and extracellular signaling pathways.¹ Accordingly, mutations in tetraspanins are the cause

*Corresponding authors. E-mail addresses:
tgonen@u.washington.edu; twalz@hms.harvard.edu.

Present addresses: T. Gonen, Department of Biochemistry, University of Washington, Seattle, WA 98195, USA; Y. Cheng, Department of Biochemistry and Biophysics, University of California San Francisco, San Francisco, CA 94158, USA.

Abbreviations used: TEM, tetraspanin-enriched microdomains; LEL, large extracellular loop; UP, uroplakin; EMP, epithelial membrane protein; EM, electron microscopy; STEM, scanning transmission electron microscopy; FSC, Fourier shell correlation; AUM, asymmetric unit membrane.

of a number of diseases, including X-linked mental retardation,³ retinal degradation^{4,5} and cataractogenesis.⁶ The diverse range of biological functions assigned to tetraspanins can be attributed to their role as transmembrane scaffolds that organize a variety of proteins into specific signaling complexes. Among the known ligands of tetraspanins are various integrins, phosphatidylinositol-4 kinase, and members of the immunoglobulin superfamily of cell surface receptors.² Since tetraspanins also interact with each other, they concentrate these signaling molecules into specialized membrane domains, known as tetraspanin webs or tetraspanin-enriched microdomains (TEMs).²

The assembly of TEMs is a poorly understood process due to the vast variability of components that can be incorporated into a single TEM. TEM assembly is thought to involve a hierarchical series of protein-protein interactions.² The lowest level of assembly is mediated through direct protein-protein contacts between multiple monomers of an individual tetraspanin or by direct interactions of a tetraspanin with one or several of its ligands. These primary interactions have been identified by cross-linking experiments and are resistant to detergents such as Triton X-100.⁷ Secondary interactions are formed between primary complexes. Secondary complexes can be composed of a single or multiple tetraspanins and can be dissociated by selected non-ionic detergents. Several reports have demonstrated that chelation of divalent metal ions weakens or disrupts secondary interactions.^{8,9} Similar effects have been observed when palmitoylation sites were ablated.⁷ Palmitoylation sites have been identified in at least eight tetraspanins, while 30 of the 32 known mammalian tetraspanins, including MP20, have membrane-proximal cysteine residues that may be potential palmitoylation sites.² Secondary order complexes can be recovered intact in low-density fractions in sucrose gradients following solubilization in mild detergents.² These low-density fractions have higher cholesterol and sphingomyelin contents than the surrounding membrane.¹⁰ Higher-order interactions between pairs of tetraspanin complexes are less well characterized due to their varied composition and large size. This hierarchy of interactions allows the tetraspanins to coordinate a vast array of membrane proteins into TEMs, which constitute functional membrane domains.

Structural information on tetraspanins and TEMs is currently still limited. The only existing high-resolution structural information of a tetraspanin domain is a crystal structure of the LEL of CD81.^{11,12} The LEL folds into a mushroom-like structure composed of five α -helices, arranged in "stalk" and "head" domains. The stalk domain contains a large hydrophobic cluster that is thought to be involved in homo- and/or heterodimerization of tetraspanins. The head domain contains a second low-polarity patch that is located in a segment, which displays enhanced residue variability among different tetraspanins. This low-polarity patch was therefore proposed to be involved in species or

tetraspanin-specific recognition processes. The only other structural information on tetraspanins comes from recent electron crystallographic data on the asymmetric unit membrane (AUM). A density map with a resolution of 6 Å provides a first ultrastructural view of how tetraspanins interact with their ligands.¹³ The AUM is found in urinary bladder epithelial cells and is composed of four membrane proteins called uroplakins (UPs) Ia, Ib, II and IIIa. UPs Ia and Ib are tetraspanins, whereas UPs II and IIIa are single-span membrane proteins. The four UPs assemble into 6-fold symmetric, star-shaped particles, with each spike composed of an inner and an outer density. The density map resolved five-helix bundles in each of the six inner and outer densities. In each of the two five-helix bundles, the transmembrane domain of the tetraspanin, either UP Ia in the inner domain or UP Ib in the outer domain, contributes four of the helices, whereas the fifth helix is the transmembrane domain of the non-tetraspanin, UP II or IIIa, respectively. The UP Ib/UP II and UP Ia/UP IIIa heterodimers associate with each other through interactions of a cytoplasmic loop of the non-tetraspanin UPs II and IIIa, demonstrating that in the AUM the tetraspanin network is not created through interactions between the tetraspanins but rather through interactions of their ligands. The UP tetraspanins thus differ from some other well-characterized tetraspanins, for which cross-linking studies revealed that the tetraspanins form homodimers, homotrimers and homotetramers.² It thus appears that formation and stabilization of different TEMs is based on different structural interactions between the tetraspanins and their ligands.

Lens-specific MP20 is a member of the PMP22/EMP/MP20 subfamily of tetraspanins,^{14,15} which also includes the peripheral myelin protein 22 (PMP22)¹⁶ and the epithelial membrane proteins (EMPs) 1 to 3.^{17,18} MP20 is the second most abundant membrane protein in lens fiber cells,¹⁹ and mutations in MP20 result in cataractogenesis and blindness.^{20,21} The precise function of MP20 in the lens remains to be elucidated. Previous studies have suggested that the protein may be involved in signaling^{22,23} and cell-cell adhesion.²⁴⁻²⁶ The ability of MP20 to interact with calmodulin, together with the identification of several phosphorylation sites on its cytoplasmic carboxy terminus,^{23,27} strengthen the notion that MP20 may contribute to signaling. *In vivo* and *in vitro*, MP20 can also bind galectin-3, a prominent cell adhesion modulator,^{24,25} presumably through an interaction with sugar moieties attached to two tryptophan residues on the first extracellular loop of MP20.²⁷ Insertion of MP20 into the plasma membrane during maturation of fiber cells correlates with a dramatic decrease in the extracellular spaces,²⁶ suggesting that MP20-galectin-3 complexes may form a novel cell-cell adhesion complex in the lens.

Here, we present the purification of MP20 from sheep lenses. The basic oligomeric state of MP20 in solution and in the membrane appears to be a

tetramer. We demonstrate that maintenance and formation of higher-order assemblies of MP20 involve divalent metal ions but also appear to require an additional, not yet identified component. Reconstitution of MP20 into native lens lipids in the presence of magnesium produced ordered two-dimensional (2D) arrays, and we present a projection map of MP20 at 18 Å resolution calculated from 2D crystals in negative stain. Upon reconstitution, MP20 also formed large oligomeric particles that are likely to contain native lipids. Random conical tilt reconstruction was used to determine the structures of the four most abundant of these MP20–lipid complexes in negative stain.

Results

Purification of MP20 from sheep lenses

In contrast to other lens membrane proteins MP20 does not adsorb well to anion or cation exchange resins. We used this characteristic to develop a negative purification strategy for MP20. Fully stripped native lens membranes (Figure 1(a), lane 1) were solubilized in decyl maltoside (DM) and centrifuged to remove the detergent-insoluble fraction (Figure 1(a), lane 2) from the detergent-soluble fraction (Figure 1(a), lane 3). The soluble material was loaded onto a MonoQ anion exchange column. While all major proteins adsorbed to the column (Figure 1(a), lane 5), more than half of MP20 did not bind to the resin and could be collected in the flow-through (Figure 1(a), lanes 4 and 6). In addition to MP20, the flow-through from the MonoQ column contained solubilized native lens membrane lipids. Since MP20 binds to hydroxylapatite but the lipids do not, this resin was used to separate native lipids (Figure 1(a), lane 7) from MP20 (Figure 1(a), lane 8). Following elution from the hydroxylapatite column,

the protein was subjected to a size exclusion chromatography step using a Superose 12 column. The protein eluted at about 16 ml, which corresponds to a molecular mass of approximately 65 kDa (Figure 1(b)) consistent with previous reports.²⁵ This purification protocol, which uses 5 mM EDTA and 5 mM EGTA in the solubilization buffer, usually yielded about 1 mg of MP20 from 100 sheep lenses. When MP20 was purified in the absence of EDTA and EGTA, similar quantities of protein were obtained, but approximately 60% of the protein eluted in the void volume of the Superose 12 column (>200 kDa), suggesting that it had formed higher-order assemblies or aggregates (Figure 1(b)). When the void volume fraction was incubated overnight with 10 mM EDTA and 10 mM EGTA and subjected again to size exclusion chromatography, the protein still eluted in the void volume (data not shown), suggesting that after solubilization higher-order MP20 species are resistant to disassembly by removal of divalent metal ions.

Characterization of detergent solubilized MP20 oligomers

To further investigate the formation of higher-order MP20 species, we used negative stain electron microscopy (EM) to analyze the size distribution of MP20 particles purified in the absence and presence of the chelators EDTA and EGTA. Images of MP20 purified in the absence of chelators that eluted in the void volume from the size exclusion column (Figure 1(b), broken line) showed aggregates, but also a population of rather homogeneous doughnut-shaped particles (Figure 2(a)). About 9000 particles were interactively selected from 50 images and classification of the particles into 100 classes revealed particles of very similar sizes and morphologies (Figure 2(a), panels 1–8). The particle had a round shape, roughly 9 nm × 9 nm in size, with a

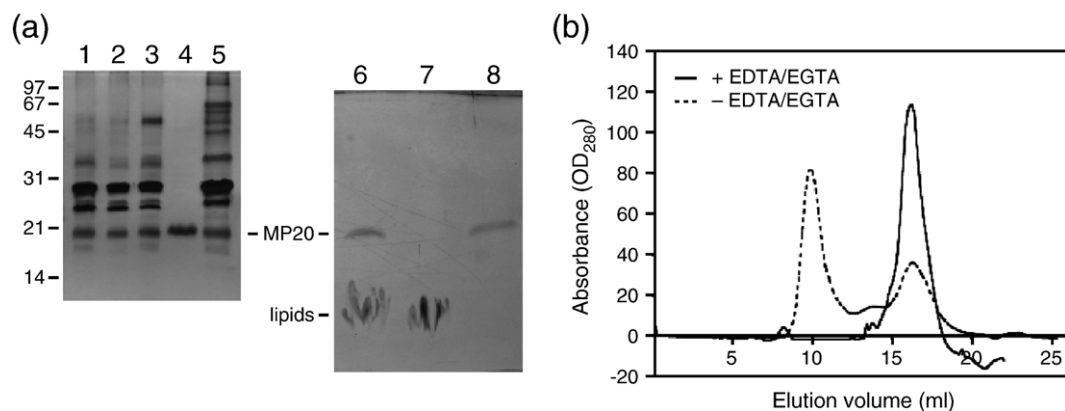


Figure 1. Purification of MP20 from sheep lenses. (a) Silver stained SDS–PAGE gels of MP20 purification; lane 1, fully stripped lens fiber cell membranes; lane 2, insoluble membrane proteins in DM; lane 3, membrane proteins solubilized in DM; lane 4, flow-through from the MonoQ anion exchange column; lane 5, elution from the MonoQ column; lane 6, flow-through from the MonoQ column; lane 7, flow-through from the hydroxylapatite column; lane 8, elution from the hydroxylapatite column. (b) Superose 12 gel filtration profiles of MP20 purified in the presence (continuous line) and absence (broken line) of EGTA and EDTA.

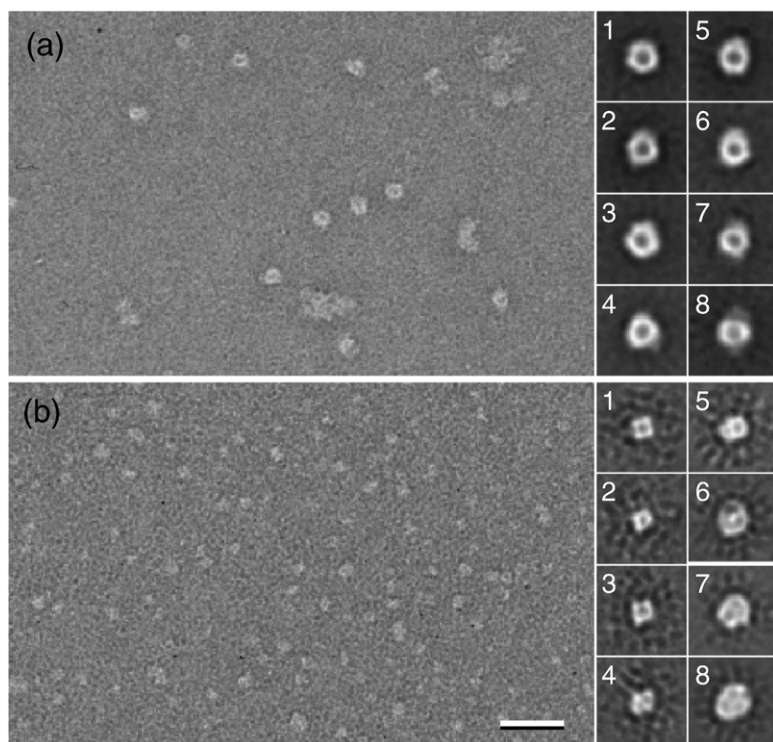


Figure 2. Negative stain electron microscopy of DM-solubilized MP20. (a) Raw image of DM-solubilized MP20 purified in the absence of EGTA and EDTA and eluted in the void volume (>200 kDa) from the Superose 12 gel filtration column. Panels 1–8 show representative class averages of the round MP20 assemblies. (b) Raw image of DM-solubilized MP20 purified in the presence of EGTA and EDTA. Panels 1–8 show representative class averages with panels 1–4 showing the predominant, square-shaped particle species and panels 5–8 examples of larger, less well-defined assemblies. The scale bar represents 20 nm. The side length of the individual panels is 22.5 nm.

central stain accumulation (Figure 2(a), panels 1–8). In contrast, despite the sharp elution peak following gel filtration (Figure 1(b), continuous line), images of MP20 purified in the presence of chelators showed a rather heterogeneous particle population. The particles appeared smaller than those purified in the absence of EDTA and EGTA (Figure 2(b)), consistent with the smaller molecular mass evident from the gel filtration profile (Figure 1(b)). When we classified about 14,000 particles interactively selected from 19 images into 200 classes, several different particle morphologies could be identified. The vast majority of the particles measured approximately 5 nm × 5 nm (Figure 2(b), panels 1–4), but some larger particles could be identified as well (Figure 2(b), panels 5–8). The smaller particles had a square shape, but several averages also showed distortions of the square shape, indicating that the arrangement of the monomers may be somewhat flexible following detergent solubilization (Figure 2(b), panels 1–4). The dimensions and shapes of these particles suggest that MP20 purified in the absence of divalent cations forms tetramers in solution, one of the oligomeric states that was identified by a cross-linking study.²⁸ The structural heterogeneity in the averages of the higher-order assemblies prevented an accurate estimate of the number of MP20 molecules, but they would be consistent with variable numbers of associated tetramers (Figure 2(b), panels 5–8). Inspection of MP20 particles purified in the absence of EGTA and EDTA that eluted from the gel filtration column at 16 ml are indistinguishable from those that eluted in the presence of EGTA and EDTA at the same position, demonstrating that the chelators used during protein purification

induce the dissociation of higher-order species into tetramers.

Next we determined whether it would be possible to induce detergent-solubilized MP20 tetramers to form higher-order species by incubation with divalent metal ions. Immediately after purification of MP20 in the presence of 2 mM EDTA and 2 mM EGTA, we split the protein into four aliquots and added (1) 10 mM MgCl₂, (2) 10 mM CaCl₂, (3) 5 mM MgCl₂ and 5 mM CaCl₂, and (4) 15 mM NaCl (final concentrations). Aliquots were taken for imaging at various time points over 24 h to follow the formation of higher-order MP20 assemblies. Visual inspection revealed that the addition of Mg²⁺ and/or Ca²⁺ failed to reproduce the 9 nm round particles or restore the ratio of larger particles to tetramers found following purification in the absence of EGTA and EDTA. The experiment was repeated at fivefold higher concentrations of divalent metal ions with similar results. Addition of NaCl, which was used as a control and to determine the influence of increased ionic strength on the formation of higher-order species, also had no effect on the particle size. To quantify the changes in higher-order MP20 species, three images of each sample were taken from grids prepared after 1 h of incubation from which about 1500 particles were selected and classified into 100 classes. The quantification confirmed that addition of Mg²⁺ or Ca²⁺ did not change the concentration of higher-order species in a significant way when compared to untreated or NaCl-treated samples. Our results thus suggest that once MP20 tetramers have been purified, the addition of divalent cations no longer influences the assembly of higher-order structures.

Reconstitution of MP20 tetramers into ordered 2D arrays

For 2D crystallization experiments we used the native lipids obtained from MP20 purifications. The lipid concentration was estimated by measuring the absorbance at 242 nm of purified lens lipids (Figure 1(a), lane 7). Purified MP20 at a concentration of 1 mg/ml was mixed with native lipids at lipid-to-protein ratios (LPRs) ranging from 0.1 to 10 (mg/mg), and the detergent was removed by slow dialysis against buffer without detergent. Dialysis was normally finished within two days with twice daily buffer exchanges, and negative stain electron microscopy (EM) was used to assess the outcome of the reconstitution experiments. MP20 incorporated into lipid membranes under all tested reconstitution conditions, but crystals only formed in the presence

of MgCl_2 at an LPR of 1. This LPR induced the formation of vesicular (Figure 3(a)) as well as tubular 2D crystals (Figure 3(b)). In most cases, the calculated power spectra revealed two sets of diffraction spots (Figure 3(c)). The presence of two diffraction lattices, which must originate from the two layers of the collapsed vesicle or tube, indicates that the entire membrane area was crystalline. The 2D crystals of MP20 have unit cell dimensions of $a=b=10.4 (\pm 0.3)$ nm ($n=30$), and the highest diffraction spot (3,4) visible in the power spectrum corresponds to a resolution of 21 Å, which is approximately the resolution limit introduced by the negative stain. The Fourier coefficients of the five best images were merged and the phases were consistent up to a resolution of 18 Å. The phase residual of the centrosymmetric spots in the resolution range from 200 Å to 18 Å was 12.9° (45° is random). Phase comparisons

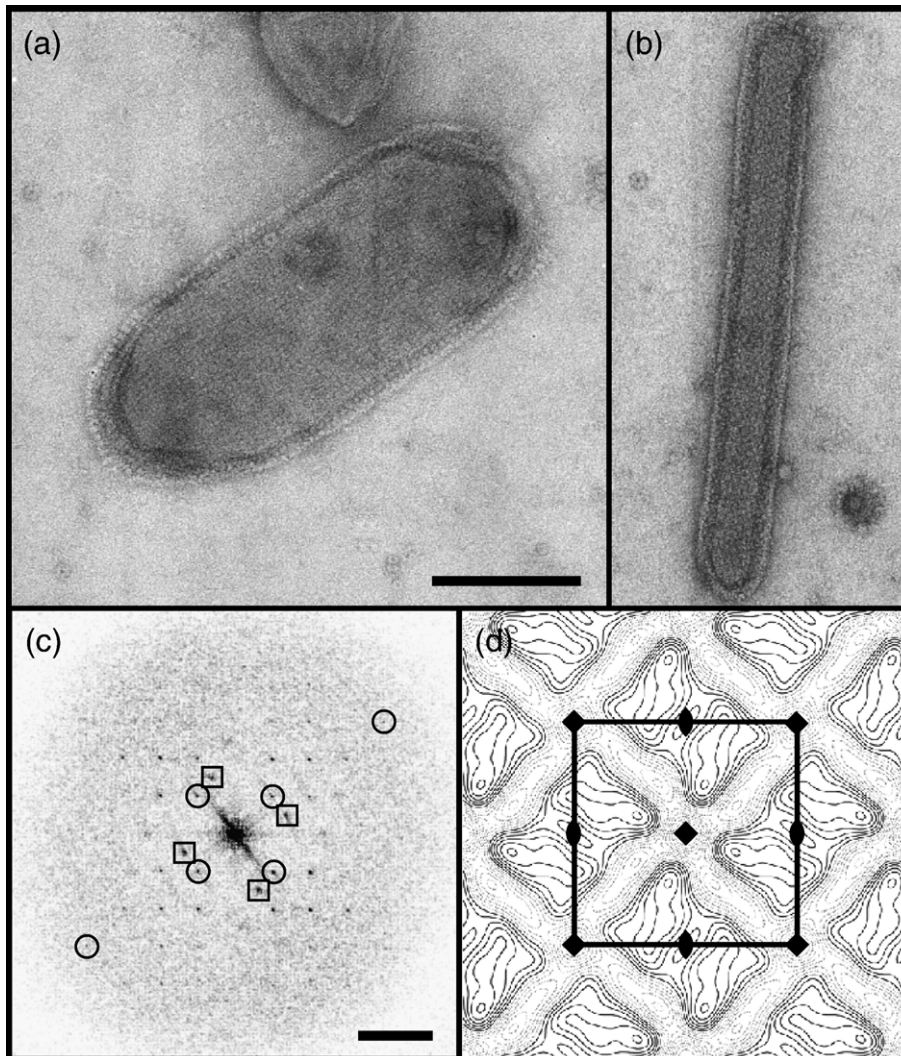


Figure 3. Negative stain electron microscopy of two-dimensional MP20 crystals. (a) Raw image of a negatively stained vesicular 2D crystal. The scale bar represents 250 nm. (b) Raw image of a negatively stained tubular 2D crystal. (c) Power spectrum of a vesicular 2D crystal. Four spots of the two different lattices are marked by circles and squares. The highest visible diffraction spot (3,4) in the power spectrum is also circled. Scale bar represents 5 nm^{-1} . (d) Projection map at 18 Å resolution calculated from the five best crystals with $p4$ symmetry imposed. A unit cell, $a=b=10.4 \text{ nm}$, $\gamma=90^\circ$, containing two rectangular densities, is outlined in black.

using the program ALLSPACE showed that the crystals have $p4$ symmetry, which was subsequently applied to calculate the 18 Å projection map shown in Figure 3(d).

Each unit cell contains two rectangular densities of $\sim 7.2 \text{ nm} \times 5 \text{ nm}$, which consist of two identical halves, related to each other by 2-fold symmetry. Assuming a thickness of the 2D crystal of 5 nm and a protein density of $0.81 \text{ Da}/\text{\AA}^3$, one of the rectangular densities would accommodate a protein mass of about 150 kDa or approximately eight MP20 molecules. The rectangular density, which is composed of two asymmetric units in the 2D crystals, is therefore most likely an octamer.

MP20 forms large oligomers in the presence of native lens lipids

In addition to the vesicular and tubular crystals, negative stain EM of the samples obtained from reconstitution experiments also revealed that large particles with a variety of morphologies adsorbed to the carbon film (Figure 4). These MP20 particles are assumed to contain lipid molecules to saturate the hydrophobic surfaces of MP20 as well as, judging from the size of the particles, a large number of MP20 molecules. These particles could be found in all reconstitution experiments with native lipids, independent of the presence of ordered 2D arrays. We collected 98 image pairs of samples tilted to 60° and 0° , from which we selected 12,163 pairs of particles. After classification of the particles selected

from the images of the untilted sample we could discern at least seven distinct types of MP20 particles (Figure 4, panels 1 to 7), all differing in size and structural features. Five types of MP20 particles showed indications of symmetry, either 6-fold (Figure 4, panels 1a 4), 3-fold (Figure 4, panel 3) or 2-fold (Figure 4, panels 2 and 7). The other particles also showed indications of symmetry, but to a much lesser extent (Figure 4, panels 5 and 6). In addition, we found round particles, which were of approximately the same size as the large 6-fold symmetric particles, but did not show any structural features, and especially did not show the large stain accumulations that are apparent in the center of the other large particles (Figure 4(a)–(d)). Although these particles appeared to display some indications of order, best seen in particle (D) in Figure 4, averages of the particle images failed to resolve any discernible fine structure (data not shown).

To better understand the morphologies of the MP20 particles, we calculated random conical tilt reconstructions of the particle classes shown in panels 1, 2, 3 and 7 in Figure 4. Closer inspection of the averages revealed that none of the particles displayed true symmetry. At this point it is not possible to judge whether the particles are truly asymmetric or whether the asymmetry was introduced by the negative staining procedure. Therefore, 3D reconstructions were calculated with and without imposing symmetry. The unsymmetrized 3D density maps of the particles confirmed that the projection averages are not just different views of the

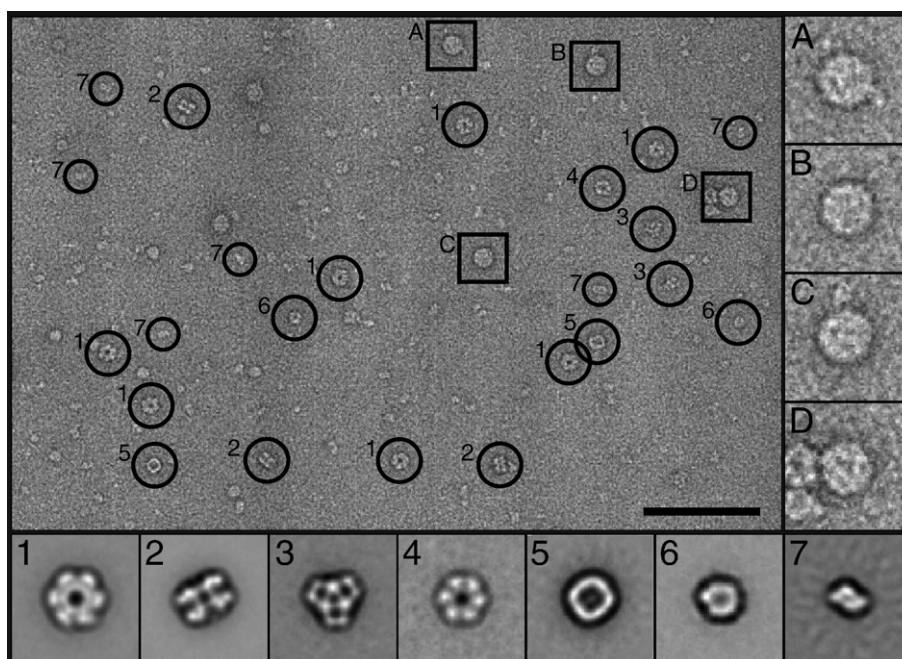


Figure 4. Negative stain electron microscopy of MP20–lipid complexes. Raw image of negatively stained MP20–lipid complexes showing the variety of particles that form upon reconstitution of MP20 with native lens lipids. Panels 1 through 7 show representative class averages of the seven most prominent particle species. Particles that correspond to each of the classes are circled and numbered in the raw image. Panels (a) through (d) are raw images of additional large particles that appear to have internal structure, which was, however, not resolved by averaging. The scale bar represents 100 nm. The side length of the individual panels is 32.3 nm.

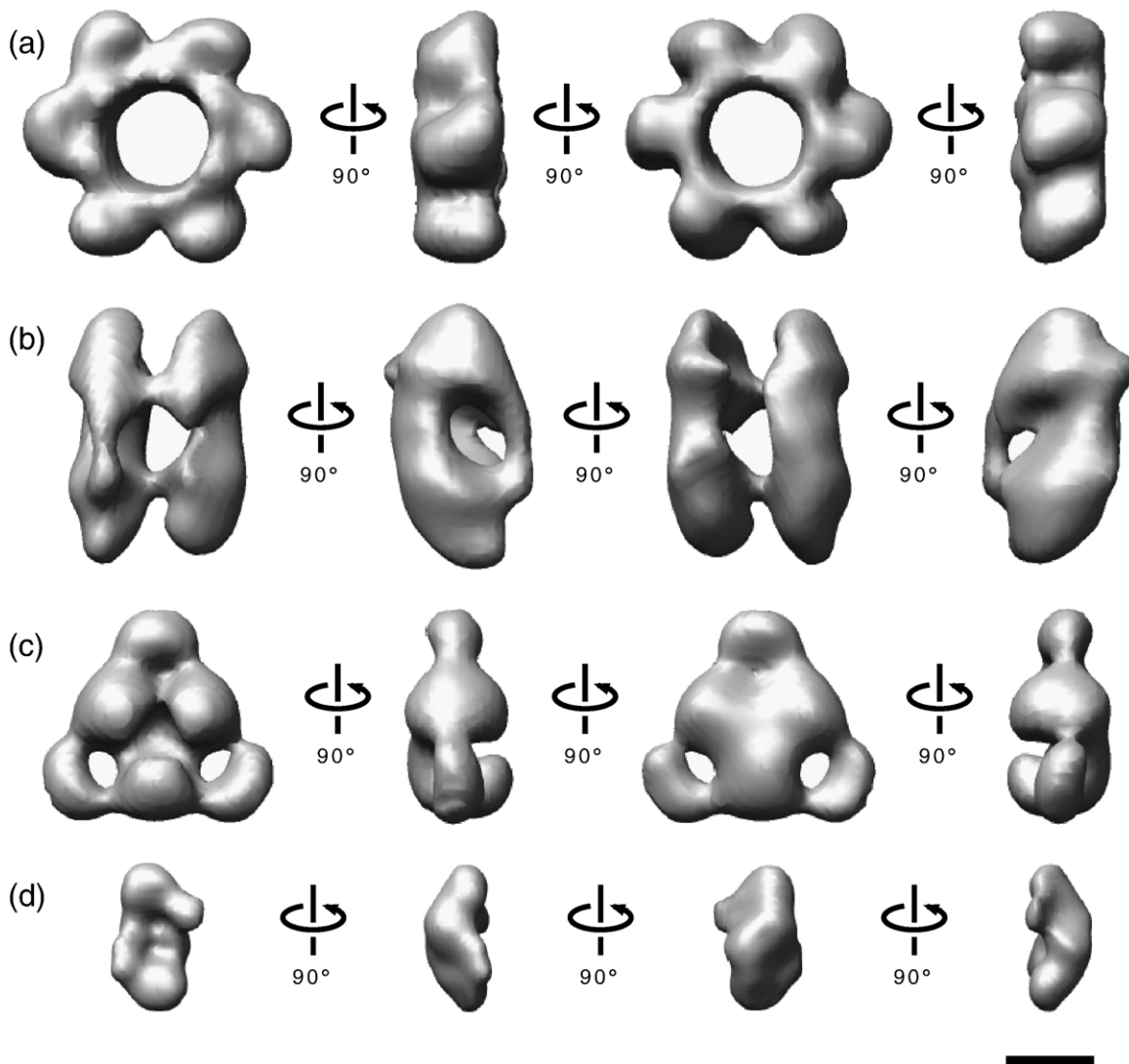


Figure 5. Three-dimensional reconstructions of negatively stained oligomeric MP20–lipid complexes. Views of the unsymmetrized density maps of (a) the six-bladed windmill particle, (b) the rectangular particle, (c) the triangular particle, and (d) the octameric particle. All reconstructions were low-pass filtered to the resolution at FSC=0.5 and thresholded to best match their corresponding projection averages. The scale bar represents 5 nm.

same particle but all represent different MP20–lipid complexes (Figure 5). The symmetrized 3D reconstructions are presented in Supplementary Data, Figure 1. The first particle has the appearance of a six-bladed windmill. It consists of six elongated domains with approximate dimensions of $5\text{ nm} \times 5\text{ nm}$. The inner and outer diameters of the particle are $\sim 4\text{ nm}$ and 15 nm , respectively (Figure 5(a)). The second particle consists of four domains, each about $3\text{ nm} \times 7\text{ nm}$ in size, which assemble into a rectangular complex with dimensions of about $9\text{ nm} \times 13\text{ nm}$ (Figure 5(b)). The third particle is triangular in shape with each side about 14 nm in length. It consists of three larger domains in the center ($\sim 4\text{ nm}$ in diameter) that are connected to three smaller and thinner peripheral domains ($\sim 3\text{ nm}$ in diameter) (Figure 5(c)). The fourth particle is the smallest, measuring approximately $10 \times 5\text{ nm}$ (Figure 5(d)). It is composed of two bi-lobed domains that appear to be related by 2-fold symmetry.

The resolutions of our 3D reconstructions, as judged by Fourier shell correlation, are between 23 \AA and 28 \AA (Supplementary Data, Figure 2). This resolution range does not suffice to distinguish molecular boundaries between the individual 20 kDa MP20 subunits, preventing us from determining the number of MP20 molecules in the different complexes. Although it is usually possible to estimate the number of subunits in a complex from the mass included in the density map, this number varies strongly with the threshold value chosen to contour the density map. This problem is compounded when a large complex is formed by a large number of small subunits and when using negative staining to prepare the samples for electron microscopy, as this preparation procedure introduces a flattening of the specimen.²⁹ Scanning transmission electron microscopy (STEM) would be an alternative approach to determine the mass of the MP20–lipid complexes. However, the limited resolution of STEM

images of unstained specimens and the lipid content of the MP20 particles rule STEM out as a means to determine the number of MP20 molecules in the various oligomers. Therefore, we can only estimate the number of subunits per particle from the size and the structural features seen in the different density maps. We estimate that the rectangular particle could contain four MP20 tetramers (16 monomers), whereas the hexagonal and the triangular particles could each contain six MP20 tetramers (24 monomers). The small size of the fourth particle allows a more accurate estimate of its composition. It measures roughly twice the length of an MP20 tetramer in solution or in the 2D crystals and it is thus likely to be an octamer composed of two tetramers.

Discussion

Our studies revealed that MP20 can assemble into a wide variety of oligomeric forms in the presence of native lens lipids. Solubilization and subsequent purification in DM in the presence of the divalent metal chelators EDTA and EGTA produced the chromatographically most homogeneous preparation, in which MP20 eluted from a size exclusion column as a single peak with an apparent molecular mass of 65 kDa (Figure 1(b)). Analysis of the protein preparation by single particle averaging revealed roughly square particles, about 5 nm × 5 nm in size (Figure 2(b), panels 1–4), along with a range of larger, less well defined particles (Figure 2(b), panels 5–8). The predominant species was composed of four equally sized densities arranged into a square (Figure 2(b), panels 1–4). The size and morphology of the small particles are thus consistent with an MP20 tetramer. The discrepancy between the expected molecular mass of a DM-solubilized MP20 tetramer (>80 kDa) and the apparent molecular mass seen by size exclusion chromatography (~65 kDa) may be assigned to a rapid equilibrium between tetramers and dimers. Dimers have been reported²⁵ but no subsequent analysis by electron microscopy was carried out. Our experiments suggest that a rapid equilibrium exists between MP20 dimers and tetramers. An MP20 dimer (~40 kDa) approaches the limit of visibility in negatively stained preparations, and so although our electron micrographs do contain some visible dimers (Figure 2(b)), these dimers are too small for single particle reconstructions.

Reconstitution of MP20 tetramers with native lens lipids produced 2D crystals. The unit cell of the crystals is composed of two rectangular densities, about 7.2 nm × 5 nm in size (Figure 3(d)). Mass calculations of these rectangular particles suggested a molecular mass of ~150 kDa, approximately twice the predicted mass of ~80 kDa for a tetramer, suggesting that two tetramers associate to form an octamer when reconstituted into the native lens lipids. The asymmetric unit of the crystals and the most common particle when solubilized are both tetramers providing additional evidence that the

tetramer is the basic oligomeric unit for MP20. There are no particles that correspond to the size and shape of the octamers among the detergent-solubilized particles, indicating that there may be a different distribution of oligomeric structures in detergent micelles and in the presence of lipids. MP20 had previously been purified in the presence of EGTA and EDTA,²⁵ but the relevance of divalent metal ion chelation in the purification protocol had not been defined. Using negative stain EM to characterize MP20 particles purified in the presence and absence of EDTA and EGTA, we found that two distinct classes of particles could be purified. Addition of the chelators yielded a population that maintained a slight degree of heterogeneity, but the heterogeneity is mostly restricted to deformations in the shape of the particles (Figure 2(b) panels 1–4). When MP20 was purified without EDTA and EGTA, some of the protein eluted from the sizing column at the same position as in the presence of chelators, but most of the protein eluted in the void volume (>200 kDa). Negative stain EM of the protein in the void volume demonstrated that the heterogeneity of MP20 in the absence of chelators is not only due to aggregation but is caused by the formation of larger, well-defined particles (Figure 2(a)). Although the class averages vary somewhat and do not resolve individual tetramers, the size (approximately 9 nm × 9 nm) and shape of these larger particles (Figure 2(a), panels 1–8), suggest that they may be composed of four MP20 tetramers. The heterogeneity of MP20 purified without chelating agents is thus caused by a tendency of MP20 tetramers to assemble into higher-order structures. Divalent metal ions appear to be necessary to stabilize interactions between tetramers during solubilization. Solubilization of lens membranes in the absence of chelating agents yields a mixed population of single tetramers and higher-order species, which consistently constituted about 60% of the purified MP20. This suggests that higher-order MP20 assemblies exist in the native lens membrane and that the degree of assembly may be defined. While divalent cations are required for association of MP20 tetramers, they do not seem to be the only factor. Once solubilized in DM, addition of divalent cations did not induce association of tetramers and chelation of divalent cations did not dissociate the higher-order assemblies. Further studies will be required to identify other factors that influence association of MP20 tetramers, which may include the native lens lipids and proteins that are lost during purification.

In addition to the tetramers and their higher-order assemblies observed in detergent solution, MP20 formed a number of even more complex assemblies upon reconstitution with native lens lipids (Figure 4). The smallest MP20–lipid complex is 2-fold symmetric and likely to represent an octamer formed by the association of two tetramers (Figure 4, panel 7). The shape and size of the octameric particle suggests that it may be structurally related to the octamers identified in the 2D crystals,

supporting the notion that lipids influence how MP20 subunits assemble. The higher-order assemblies of MP20 tetramers in detergent solution in the absence of chelators are about twice the size of the octamers, and may thus form by an association of two octamers. The lipid-containing octamer and the higher-order MP20 assemblies seen in DM are presumably the largest MP20 oligomers with physiological relevance. The resolutions of our 3D reconstructions did not suffice to visualize the arrangement of MP20 molecules in the larger MP20–lipid complexes (Figure 4, panels 1–6). However, these larger MP20–lipid complexes have complex 3D structures with variable heights (Figure 5) and are highly unlikely to form within the constraints of a planar lipid bilayer. Although these larger MP20–lipid complexes are unlikely to have physiological relevance, they illustrate that MP20 provides interaction surfaces in all three dimensions that it may utilize for association with its ligands.

Reconstitution experiments were successful only when native lens lipids were used, while all attempts to reconstitute MP20 with synthetic lipids or various natural lipid mixtures were consistently unsuccessful. During our reconstitution experiments with non-native lipids, we were unable to detect any protein in resulting vesicles and we did not see the appearance of the higher-order oligomeric species that were seen following reconstitution with native lens lipids. The composition of native lipids thus presents an ideal and possibly unique environment in which MP20 prefers to exist. The lens has a high concentration of cholesterol and sphingomyelin particularly in the lens core,³⁰ where MP20 inserts into fiber cell membranes.²⁶ Other tetraspanins also show a preference to cholesterol and sphingomyelin,¹⁰ suggesting that there is similarity between the lipid environments in which MP20 can exist and in which TEMs form. This requirement for native lipids in MP20 reconstitutions is in strong contrast to the lens-specific water channel aquaporin-0 (AQP0), which can form 2D crystals in a variety of lipids and lipid mixtures.^{31,32} MP20 is not unique, however, as other membrane proteins have been shown to crystallize exclusively in their native lipids, most notably bacteriorhodopsin.³³ Lipids can affect membrane protein structure and function^{34–36} so it is possible that MP20 together with native lens lipids form functional units whose structure is very different from detergent solubilized MP20. This possibility is strengthened by our results that show that only in the presence of lens lipids does MP20 form large oligomers such as the six-bladed windmill, rectangular and triangular species we observe (Figure 5 and Supplementary Data, Figure 1), but in the presence of DM it is predominantly a dimer/tetramer.

Reconstitution of MP20 into native lens lipids produced 2D crystals that allowed us to calculate a projection map at 18 Å resolution (Figure 3(d)). The unit cell is composed of four asymmetric densities, each of which is likely to represent an MP20 tetramer. Two symmetry-related tetramers form a

rectangular octamer presumably through protein–protein contacts, while the octamers do not appear to make direct protein–protein interactions as they are separated from each other by ~2 nm gaps in every direction. Therefore, lipids are likely to mediate the crystal contacts, which is also the case in 2D crystals formed by AQP0³¹ and may explain some of the disorder in the crystals. Unlike the AQP0 2D crystals, in which tetramers are separated by a single row of lipid molecules, the gaps between adjacent MP20 octamers would accommodate substantially more lipid molecules. The fact that the 2D crystals show paired tetramers suggests that the combination of lens lipids and divalent metal ions are sufficient to induce MP20 to associate into higher-order assemblies, although they are distinct from those particles seen after initial solubilization in the absence of EDTA and EGTA. This suggests that an additional protein factor may regulate the association of these higher-order assemblies seen prior to solubilization that is lost during further purification. In the absence of this factor, MP20 is able to adopt a wide range of oligomeric species, some of which are unlikely to be physiological.

MP20 has been classified as a member of the tetraspanin superfamily,^{14,15} and our studies show that it has indeed properties expected from a member of this family. The functional unit of MP20 appears to be a homotetramer, as has been seen for several other tetraspanins, including CD81 and CD151.² Similar to other tetraspanins, MP20 also assembles into higher-order species in a hierarchical fashion. Furthermore, the interactions leading to higher-order assemblies of MP20 tetramers are sensitive to EDTA, which has been shown to disrupt higher-order interactions of other tetraspanins.⁹ Higher-order tetraspanin interactions are also stabilized by the presence of palmitoyl groups attached to membrane proximal cysteine residues.² Although mass spectrometric analysis did not identify any palmitoylated cysteines, structure prediction suggests that MP20 contains a membrane-proximal cysteine close to the carboxy-terminal end of transmembrane domain 4²⁷ that might be amenable to palmitoylation. Despite its tetraspanin-like characteristics, MP20 is not a typical member of this family and differs in several aspects from a canonical tetraspanin. MP20 is shorter than a typical tetraspanin and it is glycosylated. More importantly, the defining large extracellular loop (LEL) of MP20 is between transmembrane domains 1 and 2 rather than between transmembrane domains 3 and 4, and the LEL does not contain the GGC sequence, which is conserved in all other tetraspanins.²⁷ Considering these differences in structure, it may be possible that lens-specific MP20 also differs in function from typical tetraspanins.

Tetraspanins are transmembrane scaffold proteins that can assemble signaling receptors into large multi-protein complexes known as TEMs. So far, no MP20-associated TEM has been reported in the lens, and no transmembrane signaling receptors have been identified that interact with MP20. Two soluble

signaling molecules, calmodulin³⁷ and galectin-3²⁵ do interact with MP20. It is thus not clear whether the significance of MP20 in the lens is at all related to TEM formation. Interestingly, MP20 is trafficked to the plasma membrane concomitantly with the loss of intracellular organelles in maturing lens fiber cells. Its insertion into the plasma membrane is also correlated with a decrease in intercellular space,²⁶ suggesting a role of MP20 in the formation of membrane junctions. Junction formation could occur through interactions with galectin-3, a prominent cell adhesion modulator.²⁵ Cell junctions play an important role in the lens, as they reduce the distance between neighboring fiber cells and thus reduce light scattering.³⁸ It is further possible that MP20 serves multiple functions on the basis that the lens is known to use the same protein for different functions, a principle known as gene sharing.³⁹ An example of gene sharing is the lens-specific water channel AQP0. This protein in its full-length form functions as a water channel,^{40,41} but cleavage of its carboxyl terminus induces the formation of a membrane junction⁴² whose structure suggests that aquaporin-0 in these junctions no longer conducts water efficiently.³¹ It is conceivable that MP20, which is the second most abundant lens membrane protein after AQP0, also serves more than one function. In cortical fiber cells, MP20 is localized to cytoplasmic vesicles prior to its insertion into the plasma membrane during differentiation.²⁶ It thus is unlikely that MP20 has a role in regulating transmembrane signaling, as the need for signaling would be reduced once fiber cells are mature and have lost their nuclei. The role of vesicular MP20 is currently unknown as are the signals that induce its trafficking to the plasma membrane. Once inserted in the plasma membrane, there are several potential components that may have a role in the regulation of the function and oligomeric state of MP20. One possible switch could be mediated by calmodulin, which is known to interact with MP20. Calmodulin has been suggested to regulate AQP0⁴³ and may also serve to regulate the functional state of MP20. Since calmodulin binds Ca^{2+} and the assembly of MP20 tetramers into higher-order species is dependent on divalent cations, different association states of MP20 may be related to calmodulin binding and activity. More work will be required to fully elucidate the functions of MP20 and how these relate to its various association states.

Materials and Methods

Purification of lens MP20

MP20 was purified following established procedures.²⁵ Briefly, sheep lenses were decapsulated, homogenized in 5 mM Tris-HCl (pH 8), 5 mM EDTA, 5 mM EGTA, and crude membranes were pelleted by centrifugation for 20 min at 30,000g. Crude membranes were resuspended in 4 M urea, 5 mM Tris-HCl (pH 9.5), 5 mM EDTA, 5 mM EGTA, and pelleted by centrifugation for 40 min at

100,000g. Membrane pellets were washed with 20 mM NaOH and stored in 5 mM Tris-HCl (pH 8), 2 mM EDTA, 2 mM EGTA at -80°C . Membranes were incubated with 1% (w/v) decyl maltoside (DM) for 30 min at room temperature in 5 mM Tris-HCl (pH 8), 2 mM EDTA, 2 mM EGTA and centrifuged at 140,000g for 30 min. Solubilized proteins in the supernatant were injected onto a MonoQ column (Pharmacia) pre-equilibrated with 0.3% DM, 5 mM Tris (pH 8), 2 mM EDTA and 2 mM EGTA. MP20, together with lens lipids, was collected in the flow-through, which was loaded on a hydroxylapatite column equilibrated with 0.3% DM in 10 mM phosphate buffer (pH 6.8), 2 mM EDTA, 2 mM EGTA. Bound MP20 was eluted with 0.5 M phosphate buffer (pH 6.8), 2 mM EDTA, 2 mM EGTA containing 0.3% DM. Purified MP20 was finally subjected to a Superose 12 (Pharmacia) size exclusion column pre-equilibrated with 0.3% DM, 5 mM Tris (pH 8), 2 mM EDTA and 2 mM EGTA. When explicitly mentioned, EDTA and EGTA were omitted from all buffers used in the purification protocol.

Effects of divalent cations on the oligomeric state of MP20 tetramers

Purified MP20 at a concentration of 0.1 mg/ml in 0.3% DM, 2 mM EDTA, 2 mM EGTA, 10 mM Tris (pH 8.0) was mixed with 1 M MgCl_2 , 1 M CaCl_2 and 1.5 M NaCl to final concentrations of 10 mM, 10 mM and 15 mM, respectively. A fourth sample was prepared that contained a final concentration of 5 mM MgCl_2 and 5 mM CaCl_2 . Samples were incubated at 4°C and aliquots were taken after 1, 12 and 24 h for inspection by negative stain EM. Samples were diluted 100-fold with the respective incubation buffer, immediately applied to EM grids, and three images were taken from each sample at each time point.

Reconstitution of MP20 with native lens lipids

Purified MP20 at a concentration of 1 mg/ml was mixed with native lens lipids at lipid-to-protein ratios (LPRs) ranging from 0.1 to 10 (mg/mg). The concentration of the native lens lipids was estimated by measuring the absorbance at 242 nm of purified native lipids. The mixtures were dialyzed against one liter of 10 mM Tris-HCl (pH 8), 100 mM NaCl, 20 mM MgCl_2 , 0.01% (w/v) NaN_3 for two days with twice daily buffer exchanges. The outcome of reconstitution experiments was assessed by negative stain EM.

Electron microscopy

All samples were prepared by conventional negative staining with 0.75% (w/v) uranyl formate as described.²⁹ All images were collected with a Tecnai T12 electron microscope (FEI, Hillsboro, OR) equipped with a LaB_6 filament and operated at an acceleration voltage of 120 kV using low dose procedures.

Images of DM-solubilized MP20 were recorded at a magnification of 67,000 \times and a defocus value of $-1.5\ \mu\text{m}$ on imaging plates. Imaging plates were read out with a DITABIS micron imaging plate scanner (DITABIS Digital Biomedical Imaging System AG, Pforzheim, Germany) using a step size of $15\ \mu\text{m}$, a gain setting of 20,000 and a laser power setting of 30%. The 2×2 pixels were averaged to yield a pixel size of $4.5\ \text{\AA}$ on the specimen level.

For the MP20–lipid complexes, image pairs at tilt angles of 60° and 0° were recorded of the same specimen areas at a nominal magnification of 52,000× and a defocus of –1.5 μm on Kodak SO-163 film. Films were developed for 12 min with full-strength Kodak D-19 developer at 20 °C. All micrographs were inspected with a laser diffractometer and only those without drift were selected for digitization with a Zeiss SCAI scanner using a step size of 7 μm. Micrographs were binned over 3×3 pixels to yield a final pixel size of 4.04 Å on the specimen level.

The best diffracting areas of images of the negatively stained 2D crystals were selected using a JEOL SF3000 laser diffractometer and 4000×4000 pixel regions were digitized with a Zeiss SCAI scanner with a step size of 7 μm. 2×2 pixels were binned to yield a pixel size of 2.7 Å on the specimen level.

Image processing

DM-solubilized MP20 particles

For MP20 purified in the presence of EGTA and EDTA, 14,069 particles were interactively selected from 19 images using WEB, the display program associated with the image processing package SPIDER,⁴⁴ which was used for all further image processing steps. The particles were windowed into 50×50 pixel images and subjected to ten cycles of multi-reference alignment. Each round of multi-reference alignment was followed by principal component analysis and K-means classification specifying 100 output classes. The references used for the first multi-reference alignment were randomly chosen from the raw images. For MP20 purified in the absence of EGTA and EDTA, 9716 particles of MP20 were interactively selected from 50 images, windowed into 64×64 pixel images and classified into 100 classes as described above.

Effects of divalent cations on the oligomeric state of MP20 tetramers

All visible particles in the three images taken of each sample were interactively selected (~1500 particles for each sample), windowed into 50×50 pixel images and classified into 100 classes as described above. To determine the number of higher oligomers we summed the number of particles in which the size of the class average exceeded 5 nm×5 nm.

MP20–lipid complexes

12,163 particle pairs were selected from 98 image pairs recorded at tilt angles of 0° and 60° using WEB. The selected particle pairs were windowed into 80×80 pixel images and the particles from the images of the untilted specimen were classified into 100 classes as described above. Four types of MP20–lipid complexes were selected for 3D reconstruction, to which we will refer as windmill, rectangular, triangular and octameric particles. Particle images from classes that showed very similar projection averages were combined (2542 windmill, 1796 rectangular, 487 triangular and 2552 octameric particles) and used for 3D reconstruction with the random conical tilt technique⁴⁵ implemented in the SPIDER package. The particles selected from the images of the tilted specimens of these classes were used to calculate initial 3D reconstructions by backprojection and backprojection refinement. The resolutions of the final 3D reconstructions were estimated using Fourier shell correlation (FSC) and

were 26 Å, 28 Å, 25 Å, and 23 Å for the windmill, triangular, rectangular and octameric particles, respectively, using the FSC=0.5 criterion.

2D crystals

Images of MP20 2D crystals were processed with the MRC suite of image processing programs⁴⁶ following well-established procedures.⁴⁷ The program ALLSPACE⁴⁸ was used to determine the two-sided plane group of the crystals.

Acknowledgements

This work was supported by NIH grant EY015107 (to T.W.). The EM facility at Harvard Medical School was established with a donation from the Giovanni Armenise Harvard Center for Structural Biology and is maintained with funds from NIH grant GM62580 (to T.W.).

Supplementary Data

Supplementary data associated with this article can be found, in the online version, at [doi:10.1016/j.jmb.2007.09.001](https://doi.org/10.1016/j.jmb.2007.09.001)

References

1. Levy, S. & Shoham, T. (2005). The tetraspanin web modulates immune-signalling complexes. *Nature Rev. Immunol.* **5**, 136–148.
2. Hemler, M. E. (2005). Tetraspanin functions and associated microdomains. *Nature Rev. Mol. Cell. Biol.* **6**, 801–811.
3. Zemni, R., Bienvenu, T., Vinet, M. C., Sefiani, A., Carrie, A., Billuart, P. *et al.* (2000). A new gene involved in X-linked mental retardation identified by analysis of an X;2 balanced translocation. *Nature Genet.* **24**, 167–170.
4. Kajiwarra, K., Berson, E. L. & Dryja, T. P. (1994). Digenic retinitis pigmentosa due to mutations at the unlinked peripherin/RDS and ROM1 loci. *Science*, **264**, 1604–1608.
5. Dryja, T. P., Hahn, L. B., Kajiwarra, K. & Berson, E. L. (1997). Dominant and digenic mutations in the peripherin/RDS and ROM1 genes in retinitis pigmentosa. *Invest. Ophthalmol. Vis. Sci.* **38**, 1972–1982.
6. Pras, E., Levy-Nissenbaum, E., Bakhan, T., Lahat, H., Assia, E., Geffen-Carmi, N. *et al.* (2002). A missense mutation in the LIM2 gene is associated with autosomal recessive presenile cataract in an inbred Iraqi Jewish family. *Am. J. Hum. Genet.* **70**, 1363–1367.
7. Kovalenko, O. V., Yang, X., Kolesnikova, T. V. & Hemler, M. E. (2004). Evidence for specific tetraspanin homodimers: inhibition of palmitoylation makes cysteine residues available for cross-linking. *Biochem. J.* **377**, 407–417.
8. Shoham, T., Rajapaksa, R., Kuo, C. C., Haimovich, J. & Levy, S. (2006). Building of the tetraspanin web: distinct structural domains of CD81 function in

- different cellular compartments. *Mol. Cell. Biol.* **26**, 1373–1385.
9. Charrin, S., Manie, S., Oualid, M., Billard, M., Boucheix, C. & Rubinstein, E. (2002). Differential stability of tetraspanin/tetraspanin interactions: role of palmitoylation. *FEBS Letters*, **516**, 139–144.
 10. Boesze-Battaglia, K., Dispoto, J. & Kahoe, M. A. (2002). Association of a photoreceptor-specific tetraspanin protein, ROM-1, with Triton X-100-resistant membrane rafts from rod outer segment disk membranes. *J. Biol. Chem.* **277**, 41843–41849.
 11. Kitadokoro, K., Bordo, D., Galli, G., Petracca, R., Falugi, F., Abrignani, S. *et al.* (2001). CD81 extracellular domain 3D structure: insight into the tetraspanin superfamily structural motifs. *EMBO J.* **20**, 12–18.
 12. Kitadokoro, K., Ponassi, M., Galli, G., Petracca, R., Falugi, F., Grandi, G. & Bolognesi, M. (2002). Subunit association and conformational flexibility in the head subdomain of human CD81 large extracellular loop. *J. Biol. Chem.* **383**, 1447–1452.
 13. Min, G., Wang, H., Sun, T. T. & Kong, X. P. (2006). Structural basis for tetraspanin functions as revealed by the cryo-EM structure of uroplakin complexes at 6-Å resolution. *J. Cell Biol.* **173**, 975–983.
 14. Louis, C. F., Hur, K. C., Galvan, A. C., TenBroek, E. M., Jarvis, L. J., Eccleston, E. D. & Howard, J. B. (1989). Identification of an 18,000-dalton protein in mammalian lens fiber cell membranes. *J. Biol. Chem.* **264**, 19967–19973.
 15. Taylor, V., Welcher, A. A., Program, A. E. & Suter, U. (1995). Epithelial membrane protein-1, peripheral myelin protein 22, and lens membrane protein 20 define a novel gene family. *J. Biol. Chem.* **270**, 28824–28833.
 16. Welcher, A. A., Suter, U., De Leon, M., Snipes, G. J. & Shooter, E. M. (1991). A myelin protein is encoded by the homologue of a growth arrest-specific gene. *Proc. Natl Acad. Sci. USA*, **88**, 7195–7199.
 17. Lobsiger, C. S., Magyar, J. P., Taylor, V., Wulf, P., Welcher, A. A., Program, A. E. & Suter, U. (1996). Identification and characterization of a cDNA and the structural gene encoding the mouse epithelial membrane protein-1. *Genomics*, **36**, 379–387.
 18. Taylor, V. & Suter, U. (1996). Epithelial membrane protein-2 and epithelial membrane protein-3: two novel members of the peripheral myelin protein 22 gene family. *Gene*, **175**, 115–120.
 19. Alcalá, J., Lieska, N. & Maisel, H. (1975). Protein composition of bovine lens cortical fiber cell membranes. *Exp. Eye Res.* **21**, 581–595.
 20. Steele, E. C., Jr, Kerscher, S., Lyon, M. F., Glenister, P. H., Favor, J., Wang, J. & Church, R. L. (1997). Identification of a mutation in the MP19 gene, Lim2, in the cataractous mouse mutant To3. *Mol. Vis.* **3**, 5.
 21. Steele, E. C., Jr, Wang, J. H., Lo, W. K., Saperstein, D. A., Li, X. & Church, R. L. (2000). Lim2(To3) transgenic mice establish a causative relationship between the mutation identified in the lim2 gene and cataractogenesis in the To3 mouse mutant. *Mol. Vis.* **6**, 85–94.
 22. Louis, C. F., Johnson, R., Johnson, K. & Turnquist, J. (1985). Characterization of the bovine lens plasma membrane substrates for cAMP-dependent protein kinase. *Eur. J. Biochem.* **150**, 279–286.
 23. Louis, C. F., Hogan, P., Visco, L. & Strasburg, G. (1990). Identity of the calmodulin-binding proteins in bovine lens plasma membranes. *Exp. Eye Res.* **50**, 495–503.
 24. Gonen, T., Donaldson, P. & Kistler, J. (2000). Galectin-3 is associated with the plasma membrane of lens fiber cells. *Invest. Ophthalmol. Vis. Sci.* **41**, 199–203.
 25. Gonen, T., Grey, A. C., Jacobs, M. D., Donaldson, P. J. & Kistler, J. (2001). MP20, the second most abundant lens membrane protein and member of the tetraspanin superfamily, joins the list of ligands of galectin-3. *BMC Cell Biol.* **2**, 17.
 26. Grey, A. C., Jacobs, M. D., Gonen, T., Kistler, J. & Donaldson, P. J. (2003). Insertion of MP20 into lens fibre cell plasma membranes correlates with the formation of an extracellular diffusion barrier. *Exp. Eye Res.* **77**, 567–574.
 27. Ervin, L. A., Ball, L. E., Crouch, R. K. & Schey, K. L. (2005). Phosphorylation and glycosylation of bovine lens MP20. *Invest. Ophthalmol. Vis. Sci.* **46**, 627–635.
 28. Jarvis, L. J. & Louis, C. F. (1995). Purification and oligomeric state of the major lens fiber cell membrane proteins. *Curr. Eye Res.* **14**, 799–808.
 29. Ohi, M., Li, Y., Cheng, Y. & Walz, T. (2004). Negative staining and image classification - powerful tools in modern electron microscopy. *Biol. Proced. Online*, **6**, 23–34.
 30. Broekhuysse, R. M. & Kuhlmann, E. D. (1972). Lipids in tissues of the eye. VI. Sphingomyelins and cholesterol esters in human sclera. *Exp. Eye Res.* **14**, 111–113.
 31. Gonen, T., Cheng, Y., Sliz, P., Hiroaki, Y., Fujiyoshi, Y., Harrison, S. C. & Walz, T. (2005). Lipid-protein interactions in double-layered two-dimensional AQP0 crystals. *Nature*, **438**, 633–638.
 32. Hasler, L., Walz, T., Tittmann, P., Gross, H., Kistler, J. & Engel, A. (1998). Purified lens major intrinsic protein (MIP) forms highly ordered tetragonal two-dimensional arrays by reconstitution. *J. Mol. Biol.* **279**, 855–864.
 33. Henderson, R. & Unwin, P. N. (1975). Three-dimensional model of purple membrane obtained by electron microscopy. *Nature*, **257**, 28–32.
 34. Jensen, T. W., Hu, B. H., Delatore, S. M., Garcia, A. S., Messersmith, P. B. & Miller, W. M. (2004). Lipopeptides incorporated into supported phospholipid monolayers have high specific activity at low incorporation levels. *J. Am. Chem. Soc.* **126**, 15223–15230.
 35. Lee, A. G. (2003). Lipid-protein interactions in biological membranes: a structural perspective. *Biochim. Biophys. Acta*, **1612**, 1–40.
 36. Lee, A. G. (2005). Cell biology: a greasy grip. *Nature*, **438**, 569–570.
 37. Swamy-Mruthinti, S. (2001). Glycation decreases calmodulin binding to lens transmembrane protein, MIP. *Biochim. Biophys. Acta*, **1536**, 64–72.
 38. Donaldson, P., Kistler, J. & Mathias, R. T. (2001). Molecular solutions to mammalian lens transparency. *News Physiol. Sci.* **16**, 118–123.
 39. Piatigorsky, J. & Wistow, G. J. (1989). Enzyme/crystallins: gene sharing as an evolutionary strategy. *Cell*, **57**, 197–199.
 40. Chandy, G., Zampighi, G. A., Kreman, M. & Hall, J. E. (1997). Comparison of the water transporting properties of MIP and AQP1. *J. Membr. Biol.* **159**, 29–39.
 41. Mulders, S. M., Preston, G. M., Deen, P. M., Guggino, W. B., van Os, C. H. & Agre, P. (1995). Water channel properties of major intrinsic protein of lens. *J. Biol. Chem.* **270**, 9010–9016.
 42. Gonen, T., Cheng, Y., Kistler, J. & Walz, T. (2004). Aquaporin-0 membrane junctions form upon proteolytic cleavage. *J. Mol. Biol.* **342**, 1337–1345.
 43. Nemeth-Cahalan, K. L. & Hall, J. E. (2000). pH and calcium regulate the water permeability of aquaporin 0. *J. Biol. Chem.* **275**, 6777–6782.
 44. Frank, J., Radermacher, M., Penczek, P., Zhu, J., Li, Y.,

- Ladjaj, M. & Leith, A. (1996). SPIDER and WEB: processing and visualization of images in 3D electron microscopy and related fields. *J. Struct. Biol.* **116**, 190–199.
45. Radermacher, M., Wagenknecht, T., Verschoor, A. & Frank, J. (1987). Three-dimensional reconstruction from a single-exposure, random conical tilt series applied to the 50S ribosomal subunit of *Escherichia coli*. *J. Microsc.* **146**, 113–136.
46. Crowther, R. A., Henderson, R. & Smith, J. M. (1996). MRC image processing programs. *J. Struct. Biol.* **116**, 9–16.
47. Amos, L. A., Henderson, R. & Unwin, P. N. (1982). Three-dimensional structure determination by electron microscopy of two-dimensional crystals. *Prog. Biophys. Mol. Biol.* **39**, 183–231.
48. Valpuesta, J. M., Carrascosa, J. L. & Henderson, R. (1994). Analysis of electron microscope images and electron diffraction patterns of thin crystals of phi 29 connectors in ice. *J. Mol. Biol.* **240**, 281–287.